Article

SERS Studies on the Dynamic Response of Membrane Interface Lipids to Proteins: Concentration Effect and Redox State Conversion

Ji Sha [1,2], Xin Wang [1], Yan Zhou [1], Yifan Chen [1], Junyi Zhao [1], Lili Cong [1,3], Jingjing Chang [2,*], and Shuping Xu [1,4,*]

[1] State Key Laboratory of Supramolecular Structure and Materials, College of Chemistry, Jilin University, Changchun 130012, China
[2] School of Chemistry and Environmental Engineering, Changchun University of Science and Technology, Changchun 130022, China
[3] Department of Gynecological Oncology, Gynecology and Obstetrics Center, The First Hospital of Jilin University, Changchun 130021, China
[4] Center for Supramolecular Chemical Biology, College of Chemistry, Jilin University, Changchun 130012, China
* Correspondence: changjingjing@cust.edu.cn (J.C.); xusp@jlu.edu.cn (S.X.)
Received: 31 March 2026; Revised: 25 May 2026; Accepted: 31 May 2026; Published: 16 June 2026

Abstract: The dynamic behavior of lipids at membrane interfaces is essential for maintaining the structural stability and functional specificity of biomembranes, with its regulation closely linked to protein interactions and the redox microenvironment. Understanding the interaction between proteins and phospholipid membranes, as well as the impact of redox processes on membrane structures, is therefore crucial for clarifying membrane functions and mechanisms. This study developed a phospholipid bilayer-on-plasmonic nanoparticle (BOM) configuration using an extruder. Based on this configuration, we conducted a systematic investigation of the dynamic interactions and concentration-dependent effects of bovine serum albumin (BSA), cytochrome c (Cyt c), and lactoferrin (LF) on zwitterionic dioleoylphosphatidylcholine (DOPC) bilayers coated silver nanoparticles (DOPC@Ag) *via* surface-enhanced Raman spectroscopy (SERS). Furthermore, by leveraging a non-physiological artificial electron-transport chain model, we elucidated the redox-dependent regulatory mechanisms of Cyt c on both synthetic phospholipid membranes and natural cellular membranes. Our observations provide insight into the lipid-protein-redox interaction network, offering suggestions for membrane biosensor design, targeted drug delivery systems, and the study of membrane-related physiological and pathological processes.

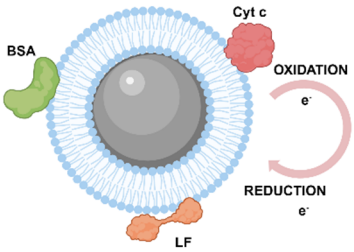

Keywords: surface-enhanced Raman spectroscopy; phospholipid membrane; lipid-protein interaction; redox; cytochrome c

1. Introduction

Biomembranes are fundamental components of cells and their internal organelles. Their inherent fluidity drives continuous processes of synthesis, remodeling, fission, and fusion [1,2]. This dynamic nature renders the biomembrane a highly adaptable compartment, providing an indispensable structural foundation for all bio units. Crucially, core cellular functions, including receptor signaling, intercellular communication, and membrane transport, rely on the precise modulation of membrane properties by key proteins (such as cytochrome c and iron transporters) and lipid components (such as cholesterol and cardiolipin) [3–5]. These molecular players exert spatiotemporal control over biomembrane function by regulating membrane fluidity, phase distribution, and curvature stress [6–8].

The analysis of lipid-protein interactions faces significant challenges with conventional techniques such as nuclear magnetic resonance (NMR) [9], infrared spectroscopy (IR) [10,11], and quartz crystal microbalance with

dissipation monitoring (QCM-D) [12]. NMR demands exceptionally high sample purity and quantity, poses challenges in establishing membrane-mimetic environments, and entails complex data interpretation. IR spectroscopy primarily yields low-resolution information on protein secondary structure and suffers from severe interferences from water vibrational bands. While QCM-D enables real-time monitoring of adsorbed mass changes and viscoelastic properties, it lacks chemical specificity and pre-identification of interacting molecular species; furthermore, its measurement of "hydrated mass" complicates quantitative analysis [13–16].

Raman spectroscopy offers distinct advantages for probing lipid-protein interactions [17]. Surface-enhanced Raman spectroscopy (SERS) combines ultra-high sensitivity with exceptional interfacial specificity, enabling not only single-molecule detection but also precise interrogation of nanoscale dynamic processes at membrane interfaces [18]. Critically, it concurrently provides real-time molecular fingerprint information, establishing a powerful tool for investigating biomembrane interfacial processes [16,19,20].

Although significant progress has been made in the studies of lipid-protein interactions, the mechanism by which the redox microenvironment orchestrates hierarchical protein-phospholipid interactions across spatiotemporal scales remains elusive [21–23]. To address this fundamental question, we constructed a phospholipid bilayer-on-metal particle (BOM) structure using an extruder and investigated its interactions with diverse proteins *via* SERS. In this study, we took dioleoylphosphatidylcholine (DOPC) to mimic the cell membrane and coated silver nanoparticles (Ag NPs) with DOPC to achieve a phospholipid bilayer-on-plasmonic nanoparticle (BOM) configuration, DOPC@Ag. Owing to the plasmonic enhancement effect of Ag NPs, the SERS spectra of DOPC bilayers can be significantly improved and analyzed in detail. Our observations revealed that the SERS behaviors of lipids are concentration-dependent in the presence of spiked proteins. Furthermore, we systematically compared the redox responses of this biomimetic DOPC@Ag system with the red blood cell membrane-on-Ag NP system (RCM@Ag). A direct causal relationship between the redox state of membrane-bound cytochrome c (Cyt c) and its regulatory function on the structure and dynamics of lipid bilayers was built. This work delineates the concentration-dependent interaction modes between three representative proteins and zwitterionic phospholipid membranes. It also elucidates the molecular mechanism by which redox-state transitions modulate dynamic processes at the lipid-protein interface, providing a valuable theoretical basis for the field of membrane redox biology. Additionally, our study demonstrates that this BOM configuration can be a powerful tool for investigating lipid-protein interactions.

2. Experimental Section

2.1. Preparation of DOPC@Ag

The 200-nm pore-size filter membrane was installed in a micro liposome extruder (as shown in Figure 1a). Subsequently, 450 μL of the DOPC vesicle solution was subjected to 11 consecutive extrusion cycles through the membrane. Following this, 500 μL of AgNP solution (~50 nm in diameter, see Supplementary Materials for more details) was passed through the same membrane. The filter membrane was then replaced with a 100-nm-pore-size membrane, and the resulting mixture was further extruded 11 times. The final product, DOPC@Ag, was collected and stored at 4 °C for future use.

2.2. Protein Assembly on DOPC@Ag

To prepare protein-conjugated DOPC@Ag complexes, DOPC@Ag was mixed with BSA in equal volumes and incubated at 37 °C for 40 min to facilitate complex assembly, then centrifuged at 5300 rpm for 10 min to remove unbound proteins. The resulting BSA-DOPC@Ag complex was resuspended in PBS for further characterization. The same procedure was repeated to prepare Cyt c-DOPC@Ag and LF-DOPC@Ag complexes.

2.3. Quartz Crystal Microbalance with Dissipation (QCM-D) Measurements

We employed QCM-D to trace the protein assembly on the DOPC membrane. First, we need a supported lipid bilayer (SLB) film on the surface of a QCM chip. To fabricate the SLB film, we prepared a bicelle solution (Stage I, Figure 2). More details for the protocols of bicelles and SLB films can be found in our previous publication [24]. Briefly, a DOPC chloroform solution was thoroughly mixed at the predetermined molar ratio. The solvent was then slowly evaporated using nitrogen blowing until the chloroform had completely evaporated, resulting in a uniform lipid film on the inner wall of the container. The lipid film was subsequently transferred to a vacuum desiccator and dried continuously for 6–8 h to remove residual organic solvents completely. The dried lipid film was hydrated with PBS buffer (pH 7.4) and vigorously shaken to form a turbid vesicle suspension. Next, short-chain lipids were added at a molar ratio of long-chain to short-chain lipids of 3:1 to construct a binary

phospholipid particle system. The mixed suspension underwent 5–10 freeze-thaw cycles (rapid freezing in liquid nitrogen for 1 min, thawing in a 60 °C water bath for 5 min, followed by vortex mixing for 30 s each time) until the solution transitioned from turbid to clear, indicating the formation of homogeneous nanostructures.

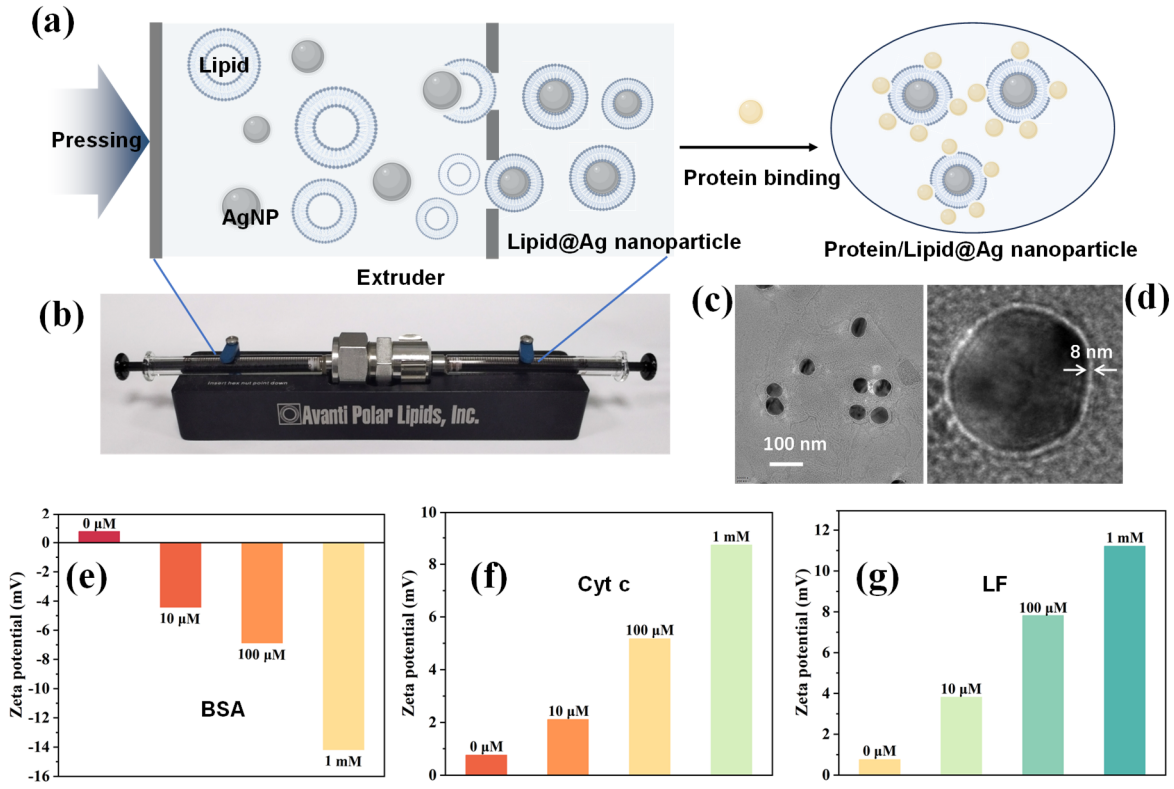

Figure 1. (**a**) Schematic diagram of phospholipid-encapsulated nanoparticles. (**b**) Liposome extruder schematic diagram. (**c**) TEM images of DOPC@Ag. (**d**) A high-magnification TEM image of a DOPC@Ag. (**e**–**g**) Zeta potential measurements of the DOPC@Ag before and after proteins (BSA, Cyt c, and LF) were loaded.

The final bicelles were injected into the QCM-D detection cell at a constant flow rate of 50 µL/min to monitor real-time changes in frequency and dissipation on the surface of the quartz crystal oscillator chip (QSX303, 5 MHz). Once the short-chain lipids were completely dissociated and washed away (Stage II, Figure 2 top panel), an intact supported DOPC bilayer was left on the chip surface (Stage III, Figure 2 top panel). The system was immediately switched to continuous perfusion with protein solutions at the same flow rate (maintaining the same flow rate). This enabled real-time monitoring of the dynamic interactions between the proteins and the lipid bilayer.

This experiment uses a modular fluid control system integrated with QCM-D technology. For fluid control, a high-precision, multi-channel peristaltic pump from the Swiss company Ismatec is used to maintain a constant sample flow rate in the flow cell. The core detection device is a Qense E4 four-channel QCM-D system from Finland Biolin Scientific AB. This system integrates a constant-temperature control unit and simultaneously performs real-time monitoring of four independent detection channels at 25.0 ± 0.1 °C. The test module uses the standard flow cell component of the system, and the liquid volume between the flow cell and the sensing chip is approximately 40 µL. Data collection was accomplished using the $QSoft_{401}$ software. The experimental data were parsed using the QTools module.

2.4. SERS Measurements

The experimental procedure involved mixing DOPC@Ag and Ag@RCM solutions with the protein solution at a 1:1 volume ratio, followed by incubation at 25 °C for 40 min to allow the complexes to self-assemble completely. A series of concentration gradient systems was systematically prepared for subsequent use. After incubation, the reaction mixtures were centrifuged (5300 rpm, 10 min) to remove unbound proteins, with the resulting precipitates being retained for further characterization.

SERS measurements were performed a confocal Raman spectrometer (T64000, HORIBA JOBIN YVON, Villeneuve d'Ascq, France) using a 532 nm excitation laser. The laser power was carefully maintained at 1 mW by a precision optical power meter. All spectral acquisitions were conducted under identical experimental conditions,

employing a single accumulation with an integration time of 20 s. Throughout the experimental process, a constant-temperature environment was rigorously maintained to ensure system stability and measurement reproducibility.

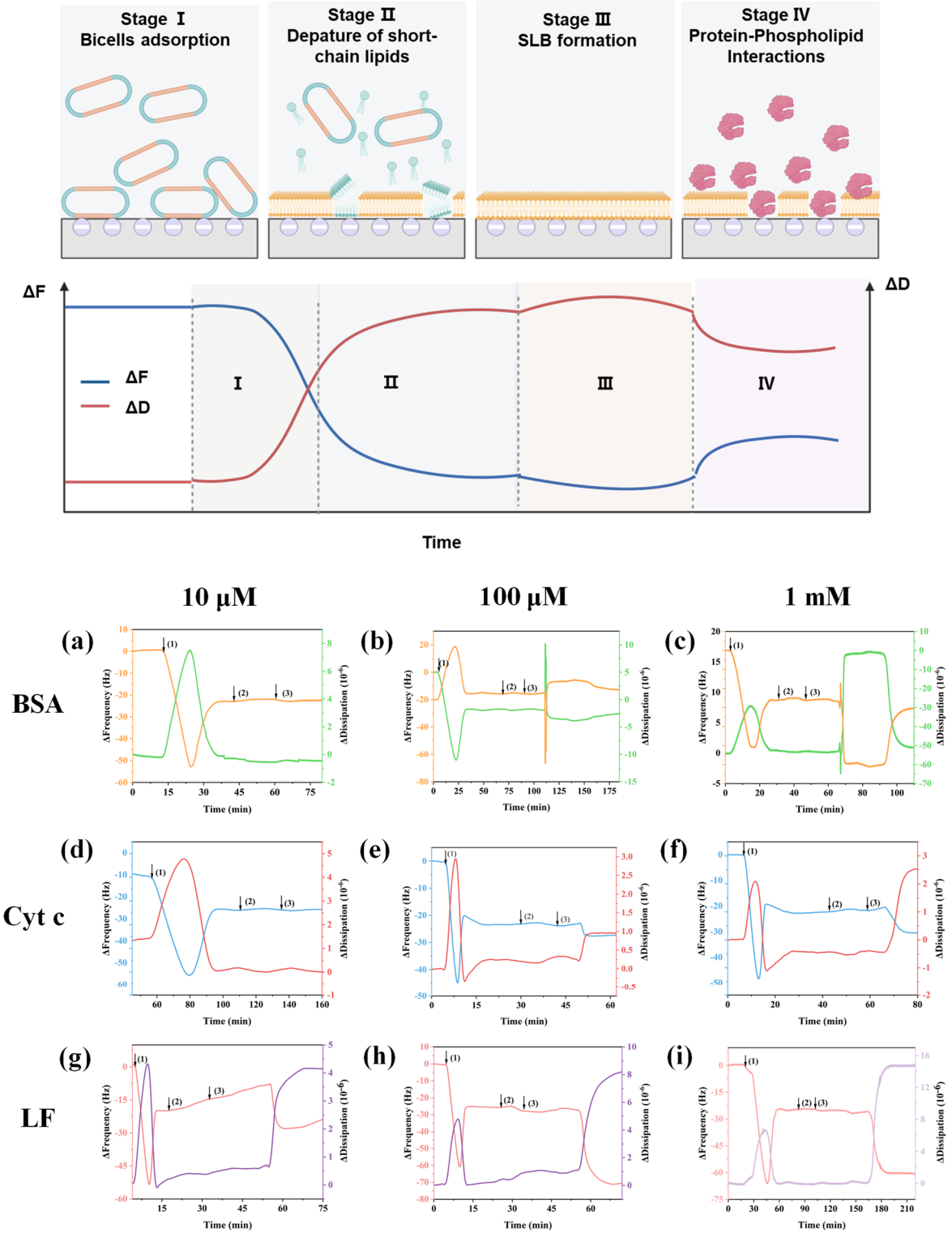

Figure 2. Schematic diagram of QCM-D analysis for protein adsorption kinetics (Top panel). QCM-D analysis of protein adsorption kinetics on DOPC (ΔF denotes the frequency variation; ΔD denotes the dissipation variation). Arrows indicate injection time points. BSA (**a**–**c**), Cyt c (**d**–**f**), and LF (**g**–**i**), respectively, with the concentration of 10 μM, 100 μM, and 1.0 M.

2.5. Spectral Processing

To quantitatively analyze the lateral packing order of lipid acyl chains, peak deconvolution fitting was performed on the C-H stretching vibration region (2800–3000 cm^{-1}). The position of the third peak, along with

the full width at half maximum (FWHM) and height of all peaks, was treated as a free parameter and iteratively optimized using the nonlinear least squares method until convergence. The spectra in this region were fitted with a Voigt profile. The peaks near 2850 and 2890 cm^{-1} correspond to the symmetric stretching vibration and asymmetric stretching vibration of the methylene group, respectively. The peak near 2927 cm^{-1} is assigned to the primary symmetric stretching vibration of methylene groups [17].

To ensure the physical significance of the fitting results and avoid overfitting, the peak positions of the three methylene vibration bands at 2848, 2890, and 2927 cm^{-1} were fixed during the fitting process, using values derived from the spectral characteristics of highly ordered pure DOPC control samples. The peak position of the third peak, as well as the full width at half maximum (FWHM) and peak height of all fitted peaks, were set as free variables. The fitting was optimized iteratively *via* nonlinear least squares until convergence. The goodness of fit was verified by a coefficient of determination ($R^2 = 0.97 > 0.95$) and the random distribution of residual plots [25,26].

3. Result and Discussion

3.1. Characterizations of Protein Assembly on DOPC@Ag

DOPC liposomes, prepared *via* the thin film hydration method [27], were mixed with the as-prepared Ag NPs. The mixture was then extruded through a polycarbonate membrane with a 100-nm pore size using a liposome extruder. Figure 1a shows schematic diagrams of phospholipid-encapsulated nanoparticles. Figure 1b is a photo of the liposome extruder used in this study. During extrusion, phospholipid molecules undergo dynamic reorganization under shear forces and membrane-pore constraints, thereby enabling the passive encapsulation of nanoparticles from the aqueous phase into the liposome bilayer and yielding the DOPC@Ag composite.

To mimic cell membranes, we decorated the DOPC@Ag with various proteins: bovine serum albumin (BSA), cytochrome c (Cyt c), and lactoferrin (LF). To verify protein interaction with electrically neutral DOPC@Ag, TEM and Zeta potential characterization were performed. Figure 1c shows TEM images of DOPC@Ag. It can be observed that DOPC was successfully coated onto the surface of Ag NPs. Figure 1d is a high-magnification TEM image. The thickness of the DOPC bilayers is 4.8 nm, indicating the successful formation of an intact phospholipid bilayer on the surface of Ag NPs. Decorating proteins on DOPC@Ag induces shifts in zeta potential upon interaction. It can be observed that negatively charged BSA decreased the potential from an initial value of −0.1 mV to −4.4 mV, −6.8 mV, and −14.2 mV at BSA concentrations of 10 μM, 10 μM, and 1.0 mM, respectively. Conversely, incubation with positively charged Cyt c and LF increased the potential to +2.1, +5.2, and +8.7 mV for Cyt c, and +3.8, +7.8, and +11.2 mV for LF as the concentration increased from 10 μM to 1.0 mM. These potential changes provide direct evidence of the protein's adsorption onto the DOPC@Ag.

To further investigate the lipid-protein interaction, QCM-D was used to monitor protein adsorption kinetics on DOPC bilayers. We first fabricated DOPC bilayers on the QCM chip using the bicelle method [24]. Next, protein solutions at different concentrations (BSA, Cyt c, and LF) were injected. The protein adsorption kinetics on DOPC bilayers were recorded, as shown in Figure 2. The measured frequency shift (ΔF) and dissipation shift (ΔD) reveal pronounced protein-specific and concentration-dependent behaviors in interfacial adsorption, membrane embedding, and structural remodeling of DOPC bilayers, with each protein exhibiting a distinct mode of action at each tested concentration (Figure 2j). At the lowest protein concentration of 10 μM, overall interactions between the proteins and DOPC membranes were negligible, with only LF yielding measurable interfacial binding. Specifically, BSA shows only trace adsorption and fails to form a stable interfacial structure (Figure 2a). For Cyt c, only a minimal decrease in ΔF and limited fluctuations in ΔD are detected, further confirming the near-absence of adsorption under this condition (Figure 2d). In contrast, LF forms a loose, stable interfacial structure *via* surface adsorption onto the phospholipid membrane, representing the only protein capable of effective interfacial binding to DOPC at 10 μM (Figure 2g).

Upon increasing the protein concentration to 100 μM, all three proteins exhibited significant interfacial interactions with DOPC membranes, albeit with fundamentally distinct interfacial structural features and molecular mechanisms. The BSA system shows a marked decrease in ΔF accompanied by a continuous increase in ΔD, a profile indicative of BSA predominantly embedding in the phospholipid bilayer *via* hydrophobic interactions and concentration-driven conformational rearrangement, establishing a dynamic adsorption equilibrium at the interface (Figure 2b). By comparison, increasing the Cyt c concentration to 100 μM results in a significant reduction in ΔF while ΔD stabilized after the initial change, suggesting the formation of a more compact interfacial layer (Figure 2e). This enhanced structural integrity is attributed to the directional insertion of the heme domain of Cyt c into the phospholipid bilayer in a vertical orientation, enabling tight association with DOPC molecules. At the same 100 μM concentration, the LF system exhibits initial dynamic profiles similar to those of BSA, namely a pronounced decrease in ΔF and a continuous increase in ΔD. However, unlike BSA, the increase

in ΔD for LF is substantially larger and sustained without reaching a plateau, indicating that LF did not achieve a stable embedded equilibrium state. Consequently, the adsorption of LF leads to a much looser, more dynamic phospholipid interface (Figure 2h).

At the highest protein concentration (1.0 mM), all three proteins induced substantial structural remodeling of the DOPC membrane, ultimately forming flexible protein-phospholipid composite interfaces, yet with marked differences in interaction strength, interfacial structural characteristics, and the underlying molecular mechanisms. BSA exhibits a distinct adsorption mode at this concentration. QCM-D monitoring reveals a continuous decrease in ΔF alongside a synchronous increase in ΔD, with both parameters eventually intersecting at a new equilibrium. These trends demonstrate that BSA is deeply embedded into the phospholipid bilayer *via* the synergistic effects of hydrophobic and electrostatic interactions, transforming the native DOPC membrane into a water-rich, soft BSA-DOPC composite interface (Figure 2c). This transition is mediated by concentration-triggered conformational rearrangement of BSA, which exposes specific functional domains and thereby markedly enhances its binding affinity to the DOPC bilayer. In contrast, Cyt c at 1.0 mM also induced a membrane softening effect, characterized by a decrease in ΔF and an increase in ΔD (Figure 2f). This phenomenon arises from a concentration-dependent transition in adsorption behavior, indicating that Cyt c formed a relatively compact, flexible interface with DOPC in dynamic equilibrium. More notably, LF at 1.0 mM triggers the most pronounced ΔF and ΔD responses among the three proteins, revealing that LF molecules induced a deeper level of structural perturbation to the phospholipid bilayer, significantly altering the assembly structure of the lipid membrane without compromising its integrity (Figure 2i). This effect stems from the high cationic charge density of LF. The dense positive charges electrostatically shield the negatively charged phospholipid headgroups, while a fraction of LF molecules can even penetrate the headgroup region into the hydrophobic core of the bilayer, inducing disordered lipid packing. Meanwhile, the formation of protein-phospholipid complexes further drives membrane curvature remodeling and redistribution of interfacial tension.

Taken together, although BSA, Cyt c, and LF all form flexible composite interfaces with DOPC at 1.0 mM, their interaction strengths and molecular mechanisms are fundamentally distinct. In short, BSA acts primarily *via* conformational rearrangement-mediated membrane embedding, Cyt c relies on directional insertion of its heme domain as the core binding mode, and LF induces the most significant interfacial softening through strong electrostatic interactions, hydrophobic insertion, and global structural perturbation of the bilayer. These distinct molecular interaction modes—weak adsorption, conformationally regulated membrane embedding, charge screening, and hydrophobic insertion—exhibit characteristic interfacial stability profiles across the protein concentration gradient. Elucidating these molecular mechanisms provides a critical theoretical foundation for the precise regulation of protein-phospholipid interactions.

These distinct concentration-dependent and protein-specific interaction behaviors observed by QCM-D are fully consistent and quantitatively correlated with the SERS results as described in Section 3.2. The mass adsorption, membrane embedding, and structural remodeling processes, as revealed by changes in ΔF and ΔD, directly induce lipid chain disordering, packing variation, and fluidity modulation, as quantified by the SERS lateral order parameter (S_{lat}). Specifically, QCM-D provides the dynamic kinetic evidence of how proteins interact with the membrane over time, while SERS offers the molecular structural evidence of how lipids respond to protein binding at the atomic level. Together, they establish a complete and multi-scale mechanistic description of lipid-protein interactions.

3.2. SERS Characterization of protein assembly on DOPC bilayer

By analyzing the characteristic spectral peaks of phospholipids, such as phosphatidylcholine and phosphatidylethanolamine, we can accurately assess membrane structural stability [28,29]. Spectral analysis combined with multidimensional data models can reveal associations between abnormal phospholipid metabolism and cardiovascular and neurodegenerative diseases, facilitating biomarker discovery and early diagnosis [30]. Thus, studies on the spectral nature of phospholipids using Raman analysis have always attracted considerable attention [31]. However, normal Raman usually provides low signals of analytes. To amplify the Raman signal of lipids, we developed a unique phospholipid bilayer-on-metal particle (BOM) configuration using an extruder. Owing to the phospholipid being close to the plasmonic nanoparticle, the short-range and long-range enhancement effects are both involved, which significantly amplify the Raman scattering signals of the phospholipid. Thus, we can further explore protein-induced phospholipid disturbances using high-quality SERS spectra of phospholipids obtained with the BOM configuration.

To directly verify and mechanistically explain the protein-induced membrane structural changes observed by QCM-D at the molecular level, SERS was employed to monitor the lipid acyl chain ordering and packing density.

The SERS results are in excellent agreement with QCM-D observations. The adsorption, insertion, and interfacial remodeling behaviors identified by frequency and dissipation shifts directly correspond to the changes in lipid chain conformation and membrane fluidity revealed by SERS. Accordingly, we correlated the QCM-D kinetic trends with the SERS spectral features and the quantitative S_{lat} values for each protein across all tested concentrations.

To investigate the effects of proteins at distinct binding sites on phospholipids, the lateral interaction order parameter [S_{lat}; see Formula (1)] was calculated from the ratio defined in Formula (2). S_{lat} quantifies both the strength of lateral interactions between phospholipid chains and the degree of chain ordering [17,28].

$$S_{lat} = \frac{I_{CH_2} - 0.7}{1.5} \tag{1}$$

$$I_{CH_2} = \frac{I_{2890}}{I_{2850}} \tag{2}$$

S_{lat} was calculated from the Raman peak intensity ratio I_{2890}/I_{2850}. All data represent the mean ± standard deviation of three independent experiments. The mean and variance of the I_{2890}/I_{2850} ratio are shown in Supplementary Figure S1.

Comparative analyses of the data in Figure 3g–i and Table 1 indicate that LF exhibits unique membrane interactions, fully supported by QCM-D results. Here, QCM-D provides real-time, quantitative information on the kinetics and thermodynamics of protein adsorption, as well as the viscoelastic properties of the resulting interfacial layer. SERS provides molecular-level insight into the structural changes in lipid molecules induced by protein binding, directly linking macroscopic interfacial properties to microscopic molecular conformations. At the trial of 10 μM LF, QCM-D shows that LF was the only protein capable of effective interfacial binding to DOPC (Figure 2g), corresponding to a remarkable 380% increase in S_{lat} in SERS—far higher than BSA (50%) and Cyt c (205%) at the same concentration. This confirms that LF has superior membrane-binding affinity even at low concentrations. In the case of 100 μM LF, ΔD for LF increased substantially and sustained without reaching a plateau (Figure 2h), indicating a much looser, more dynamic phospholipid interface. This corresponds to a further increase in S_{lat} to 400%, consistent with the continuous structural perturbation observed by QCM-D. As for the result of 1.0 mM LF, it can be observed that LF triggers the most pronounced ΔF and ΔD responses among the three proteins (Figure 2i), corresponding to an extraordinary 995% increase in S_{lat}. This demonstrates that LF molecules induce the deepest structural perturbation of the phospholipid bilayer, significantly altering lipid membrane assembly without compromising its integrity. This effect stems from the high cationic charge density of LF. The dense positive charges electrostatically shield the negatively charged phospholipid headgroups, while a fraction of LF molecules penetrate the headgroup region into the hydrophobic core of the bilayer, inducing disordered lipid packing. This is corroborated by the QCM-D signal, which indicates an increase in intact membrane mass. This observed diversity in protein-membrane interactions and their specific concentration dependencies provides multi-dimensional experimental insights into the mechanisms of biomacromolecular transmembrane transport. Taken together, the QCM-D and SERS results are fully consistent and mutually reinforcing.

The correlation between ΔF/ΔD trends and S_{lat} values across all three proteins and all concentrations confirms that both techniques are measuring the same underlying protein-membrane interaction processes. This cross-validation significantly strengthens the reliability of our conclusions and provides a comprehensive understanding of how different proteins interact with phospholipid membranes.

Table 1. S_{lat} variation rates in protein/DOPC@Ag assembly systems at varying concentrations.

Specimen	I_{2890}/I_{2850}	S_{lat}	S_{lat} Change Rate/%
DOPC@Ag	0.90 ± 0.02	0.13 ± 0.01	
10 μM BSA/DOPC@Ag	1.00 ± 0.04	0.20 ± 0.03	50.0
100 μM BSA/DOPC@Ag	1.66 ± 0.09	0.64 ± 0.06	380.0
1.0 mM BSA/DOPC@Ag	1.26 ± 0.06	0.37 ± 0.04	180.0
10 μM Cyt c/DOPC@Ag	1.31 ± 0.03	0.41 ± 0.02	205.0
100 μM Cyt c/DOPC@Ag	1.30 ± 0.04	0.40 ± 0.03	200.0
10 μM LF/DOPC@Ag	1.66 ± 0.04	0.64 ± 0.03	380.0
100 μM LF/DOPC@Ag	1.7 ± 0.03	0.67 ± 0.02	400.0
1.0 mM LF/DOPC@Ag	2.89 ± 0.03	1.46 ± 0.02	995.0

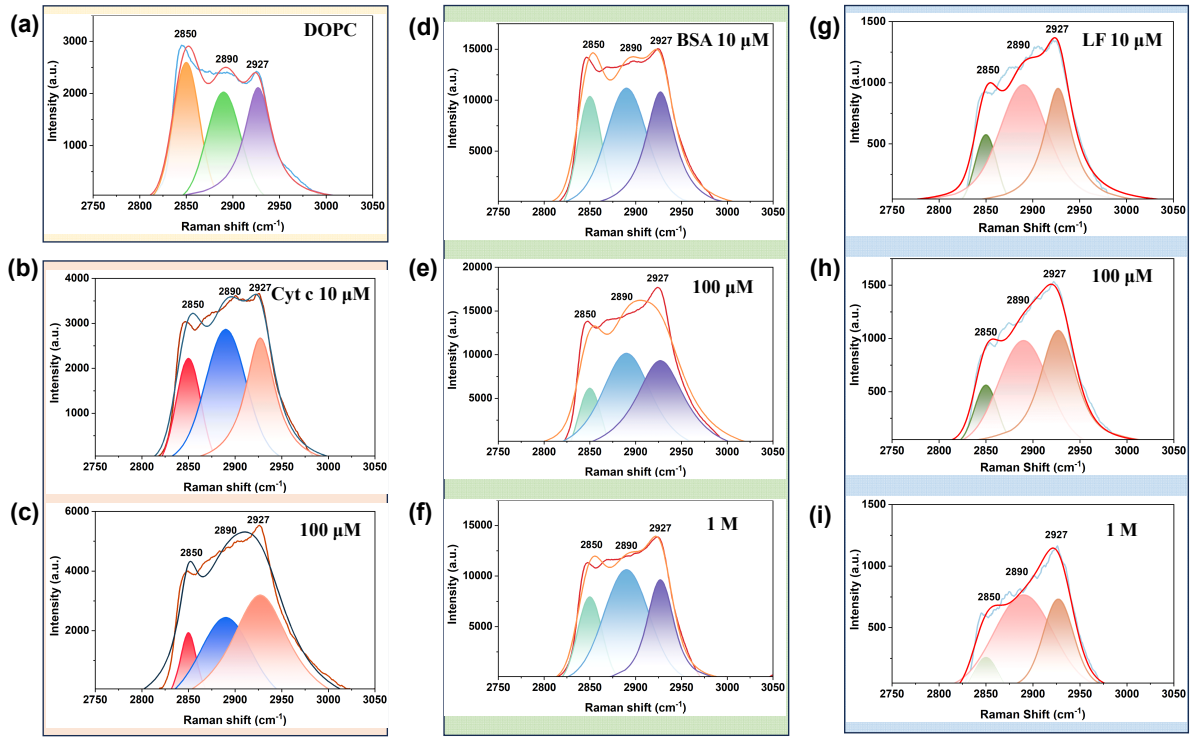

Figure 3. SERS spectra of DOPC@Ag (**a**) upon exposure to different proteins corresponding to BSA (**b**,**c**), Cyt c (**d**–**f**), and LF (**g**–**i**), with the concentration of 10, 100 μM, and 1.0 mM, respectively.

3.3. SERS Characterizations of Redox State Transitions of Cyt c on DOPC@Ag and RCM@Ag

We further investigated lipid behavior at the membrane interface during redox-state transitions. The significant attenuation of the characteristic peak at 1635 cm^{-1} serves as a key indicator of Cyt c reduction [32,33]. Figure 4a demonstrates that Cyt c immobilized on the DOPC@Ag nanocomposite surface remains fully reduced across the NADPH concentration range of 25~200 μM. Notably, at an NADPH concentration of 50 μM, Figure 4b–d shows a significant peak in the S_{lat} parameter for the phospholipid (Table 2), corresponding to an approximately 2.4-fold increase relative to the control group. This phenomenon elucidates the regulatory mechanism by which Cyt c-mediated redox reactions influence lipid-protein interfacial dynamics. During electron transfer, conformational changes in Cyt c likely attenuate van der Waals interactions between adjacent lipid acyl chains. This attenuation promotes an increase in the proportion of gauche conformers relative to all-trans conformers within the acyl chains, thereby reducing the lateral packing order. This molecular-level structural reorganization decreases the lateral packing density of the phospholipid membrane, inducing a localized relaxation effect within the bilayer microstructure. This dynamically modulated membrane environment significantly enhances fluidity and, crucially, establishes a low-energy-barrier interface conducive to conformational transitions of membrane-associated proteins and transmembrane substrate transport. Collectively, these structural adaptations likely underpin the system's superior performance in biosensing and targeted delivery applications. The S_{lat} parameter was calculated using the intensity ratio (I_{2890}/I_{2850}) of the characteristic vibrational bands at 2890 cm^{-1} (CH_2 antisymmetric stretching mode and 2850 cm^{-1} (CH_2 symmetric stretching mode). The mean and variance of the I_{2890}/I_{2850} ratio are shown in Supplementary Figure S2.

Table 2. Percentage change in S_{lat} of DOPC@Ag following Cyt c reduction at varying NADPH concentrations.

NADPH (μM)	I_{2890}/I_{2850}	S_{lat}	S_{lat} Change Rate/%
0	1.26 ± 0.04	0.37 ± 0.03	
25	1.36 ± 0.02	0.44 ± 0.01	17.9
50	2.03 ± 0.09	0.89 ± 0.06	137.5
100	1.64 ± 0.05	0.63 ± 0.03	67.9
200	1.46 ± 0.04	0.51 ± 0.03	35.7

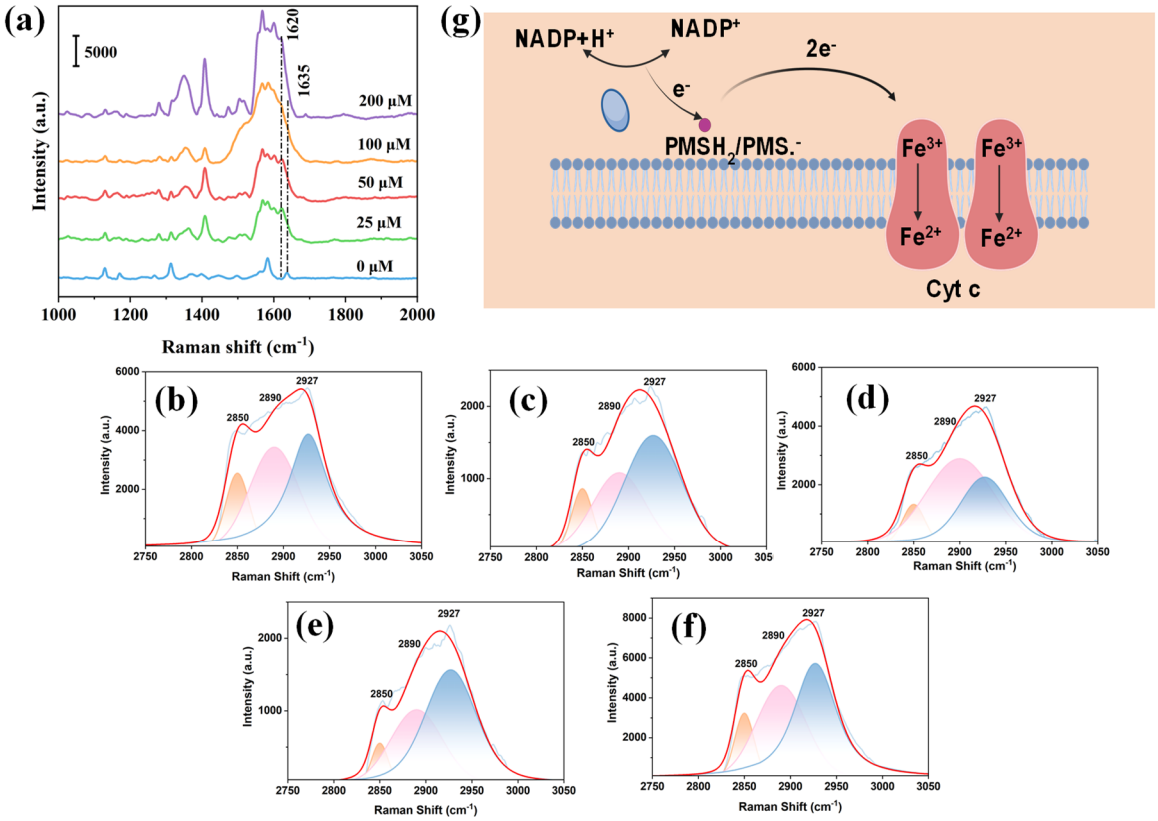

Figure 4. In situ monitoring of Cyt c redox state transformation *via* SERS. (**a**) SERS of lipids in the reduction process of cytochrome c adsorbed on DOPC@Ag. (**b**–**f**) respectively, with the concentration of 0, 25, 50, 100, and 200 μM NADPH. (**g**) The redox state transformation diagram of Cyt c.

To further verify the aforementioned conclusion regarding Cyt c redox states, we fabricated RCM@Ag from red blood cells and investigated its Cyt c redox states using SERS. RCM@Ag with an identical structure was prepared using readily available natural red blood cell membranes (RCM). As evidenced by the TEM results (Figure S3), the erythrocyte membrane prepared by the extrusion method successfully formed a homogeneous coating layer on the surface of Ag NPs. DLS characterization of the nanocomposite system (Figure S4a,b) reveals that upon RCM coating, the hydrodynamic diameter of the Ag NPs increased from 44 nm to 50 nm, while the surface zeta potential decreased significantly from −18 mV to −3.3 mV. This concurrent increase in size and reduction in surface charge indicates the formation of a stable erythrocyte membrane coating on the nanoparticle surface, mediated by electrostatic interactions. Notably, following the electrostatic assembly of Cyt c, the hydrodynamic diameter further increased to 58 nm, and the zeta potential rebounded to +2.9 mV. This charge strongly demonstrates the successful electrostatic anchoring of Cyt c onto the negatively charged cell membrane surface. The successful assembly of Cyt c on the erythrocyte membrane surface is confirmed, in good agreement with the above spectroscopic analysis, particle size, and zeta potential characterization (Figure S4).

The same spectral processing was applied to RCM@Ag, and the mean and variance of the I_{2890}/I_{2850} ratio are shown in Figure S5. Figure 5c–g demonstrate that surface-loaded Cyt c within a nanocomposite system undergoes a reduction reaction under a gradient NADPH concentration of 0–200 μM. Notably, at an NADPH concentration of 50 μM, the S_{lat} exhibited a significant response, with its relative change rate approximately 4.6-fold higher than that of the blank system (Table 3). This response quantitatively aligns with observations in the DOPC@Ag biomimetic membrane system (where the S_{lat} change rate increased by 2.4-fold), further confirming a universal regulatory mechanism whereby Cyt c-mediated redox reactions modulate phospholipid interfacial dynamics. System evidence suggests that Cyt c conformational changes during electron transfer influence membrane structure through two synergistic pathways: (1) charge fluctuations at its redox center directly weaken van der Waals interactions between acyl chains, and (2) increased rotational freedom of the heme prosthetic group induces local hydrodynamic perturbations. These effects systematically elevate the proportion of gauche conformers within the acyl chains. This molecular-scale dynamic restructuring reduces the lateral packing density of the phospholipid bilayer, forming a metastable, relaxed interfacial domain. Crucially, the higher S_{lat} responsivity observed in the native membrane system (3.1-fold vs. 2.4-fold) is likely attributable to cholesterol modulation. The rigid steroid

ring of cholesterol generates enhanced steric hindrance relaxation, thereby significantly amplifying the change in the order parameter [34–36]. This consistency in behavior between biomimetic and native systems provides a key theoretical basis for designing nanobiodevices that precisely regulate membrane environments.

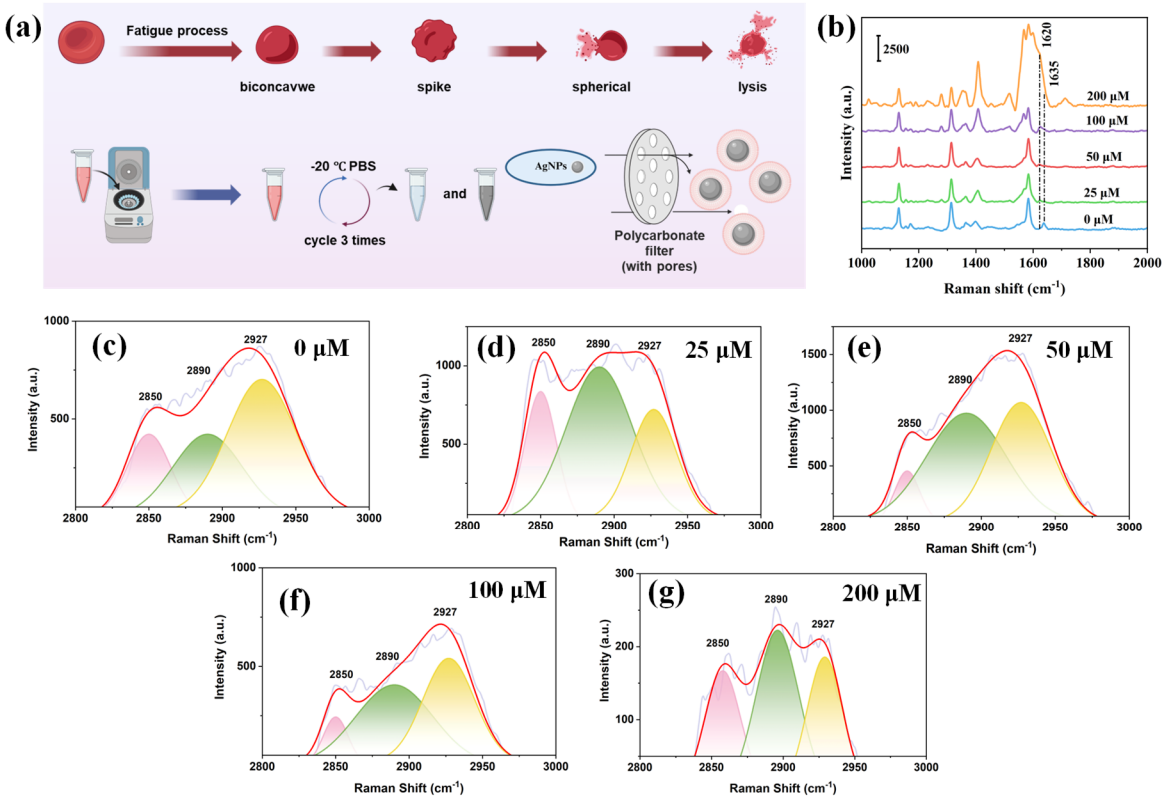

Figure 5. (**a**) Preparation flow chart of RCM@Ag. (**b**) SERS of lipids in the reduction process of Cyt c adsorbed on RCM@Ag. (**c**–**g**) respectively, with the NADPH concentrations of 0, 25, 50, 100, and 200 μM.

Table 3. Percentage changes in S_{lat} of RCM@Ag following Cyt c reduction at varying NADPH concentrations.

NADPH (μM)	I_{2890}/I_{2850}	S_{lat}	S_{lat} Change Rate/%
0	1.04 ± 0.03	0.23 ± 0.02	
25	1.20 ± 0.03	0.33 ± 0.02	47.0
50	2.09 ± 0.11	0.93 ± 0.07	308.8
100	1.58 ± 0.04	0.59 ± 0.03	158.8
200	1.49 ± 0.02	0.53 ± 0.01	132.3

4. Conclusions

We systematically elucidated the dynamic interaction mechanisms and concentration-dependent behaviors of BSA, Cyt c, and LF with DOPC phospholipid bilayers. Key findings reveal distinct protein-specific binding modes: BSA embeds in the hydrophobic membrane core *via* hydrophobic interactions, exhibiting weak adsorption at low concentrations and triggering deep insertion, acyl chain loosening, and the formation of flexible interfacial layers at high concentrations. Cyt c demonstrates orientation-dependent binding anchoring to polar headgroups *via* its heme moiety at low concentrations, while undergoing hydrophobic insertion that drives membrane softening and formation of a relatively compact yet flexible interface at elevated concentrations. LF exhibits concentration-dependent binding through strong electrostatic interactions and hydrophobic insertion, significantly enhancing lipid chain fluidity without compromising membrane integrity. Furthermore, the order parameter for lateral interactions of phospholipids S_{lat} (I_{2890}/I_{2850}) is established as a sensitive probe for quantifying phospholipid bilayer order, providing a novel basis for analyzing protein-membrane dynamic equilibria. Notably, the study reveals the redox-responsive behavior of Cyt c in both biomimetic (DOPC@Ag) and real cell membrane (RCM@Ag) systems, detailing its regulatory mechanism at the membrane interface. Redox reactions weaken van der Waals forces between acyl chains, increase gauche conformer populations, and reduce membrane lateral packing density. Comparative analysis highlights that cholesterol-mediated synergistic steric hindrance in real cell membranes significantly amplifies this interfacial remodeling. Collectively, this work elucidates the intrinsic molecular link between redox-

state transitions and membrane dynamic remodeling, providing a crucial theoretical foundation for designing redox-responsive biosensors and developing targeted delivery systems that leverage enhanced membrane fluidity.

Supplementary Materials: The following supporting information can be downloaded at: https://media.sciltp.com/articles/others/2606161457297769/MI-26030236-SM.pdf. Figure S1. Normalized I_{2890}/I_{2850} ratio of DOPC@Ag treated with BSA, Cyt c, and LF at varying concentrations. Data are normalized to pure DOPC@Ag and presented as mean ± SD (n = 3). The ratio refers to the Raman peak intensity ratio I_{2890}/I_{2850}. Figure S2. Normalized I_{2890}/I_{2850} lipid ratio of DOPC@Ag during the reduction of adsorbed Cyt c. Data are normalized to pure DOPC@Ag and presented as mean ± SD (n = 3). The ratio refers to the Raman peak intensity ratio of lipid acyl chains at 2890 cm^{-1} and 2850 cm^{-1}. Figure S3. TEM images of RCM@AgNPs. Figure S4. (a) Zeta potential of Cyt c assembled RCM@AgNPs; (b) Size distribution of Cyt c assembled RCM@AgNPs. Figure S5. Normalized I_{2890}/I_{2850} lipid ratio of RCM@Ag during the reduction of adsorbed Cyt c. Data are normalized to pure RCM@Ag and presented as mean ± SD (n = 3). The ratio refers to the Raman peak intensity ratio of lipid acyl chains at 2890 cm^{-1} and 2850 cm^{-1}. Reference [37] are cited in supplementary materials.

Author Contributions: J.S. and S.X.: conceived the idea; J.S. and Y.C.: conducted material preparation and characterizations; X.W. and Y.Z.: performed TEM image and zeta potentials; J.Z.: designed the QCM experiment; J.S. and L.C.: performed the SERS experiment; J.S.: wrote the paper; J.C. and S.X.: supported the research with funding and supervision; S.X.: revised the draft. All authors have read and agreed to the published version of the manuscript.

Funding: This research was funded by National Natural Science Foundation of China (22373041), Science Challenge Project (TZ2025011), National Key Research and Development Program of China (2023YFC3706002), the Fundamental Research Funds for the Central Universities, Joint University-Enterprise Research Project of Changchun University of Science and Technology (KYC-MX-XM-2025-021), and Innovative Research Project of State Key Laboratory of Supramolecular Structure and Materials.

Data Availability Statement: The data that support the findings of this study are available from the corresponding author upon reasonable request.

Conflicts of Interest: The authors declare no conflicts of interest regarding the publication of this paper.

Use of AI and AI-Assisted Technologies: No AI tools were utilized for this paper.

References

1. Jelokhani-Niaraki, M. Membrane proteins: Structure, function and motion. *Int. J. Mol. Sci.* **2022**, *24*, 468.
2. Vance, J.A.; Devaraj, N.K. Membrane mimetic chemistry in artificial cells. *J. Am. Chem. Soc.* **2021**, *143*, 8223–8231.
3. Almén, M.S.; Nordström, K.J.; Fredriksson, R.; Schiöth, H.B. Mapping the human membrane proteome: A majority of the human membrane proteins can be classified according to function and evolutionary origin. *BMC Biol.* **2009**, *7*, 50.
4. Kusumi, A.; Nakada, C.; Ritchie, K.; Murase, K.; Suzuki, K.; Murakoshi, H.; Kasai, R.S.; Kondo, J.; Fujiwara, T. Paradigm shift of the plasma membrane concept from the two-dimensional continuum fluid to the partitioned fluid: High-speed single-molecule tracking of membrane molecules. *Annu. Rev. Biophys. Biomol. Struct.* **2005**, *34*, 351–378.
5. Simons, K.; Gerl, M.J. Revitalizing membrane rafts: New tools and insights. *Nat. Rev. Mol. Cell Biol.* **2010**, *11*, 688–699.
6. Fajardo, V.A.; McMeekin, L.; LeBlanc, P.J. Influence of phospholipid species on membrane fluidity: A meta-analysis for a novel phospholipid fluidity index. *J. Membr. Biol.* **2011**, *244*, 97–103. https://doi.org/10.1007/s00232-011-9401-7.
7. Crosio, M.A.; Wilke, N. The neutral Red probe location in large unilamellar vesicles: Influence of membrane composition and phase states. *J. Photochem. Photobiol. A Chem.* **2024**, *452*, 163–171. https://doi.org/10.1016/j.jphotochem.2024.115615.
8. Bahja, J.; Dymond, M.K. Does membrane curvature elastic energy play a role in mediating oxidative stress in lipid membranes? *Free Radic. Biol. Med.* **2021**, *171*, 191–202. https://doi.org/10.1016/j.freeradbiomed.2021.05.021.
9. Anitha, S.; Jayasree, R.; Kulanthaivel, L.; Subbaraj, G.K.; Muthuvel, R. Advanced techniques for analyzing the protein–lipid interactions. In *Biochemical Techniques for Analyzing Protein-Lipid Interactions*; Patel, A., Ed.; Springer Nature Singapore: Singapore, 2024; pp. 157–175.
10. Arrondo, J.L.R.; Goñi, F.M. Chapter 13 Infrared Spectroscopic Studies of Lipid-Protein Interactions in Membranes. In *New Comprehensive Biochemistry*; Watts, A., Ed.; Elsevier: Amsterdam, The Netherlands, 1993; Volume 25, pp. 321–349.
11. Tatulian, S.A. Analysis of protein–protein and protein–membrane interactions by isotope-edited infrared spectroscopy. *Phys. Chem. Chem. Phys.* **2024**, *26*, 21930–21953. https://doi.org/10.1039/D4CP01136H.
12. Heider, S.; Reimhult, E.; Metzner, C. Real-time analysis of protein and protein mixture interaction with lipid bilayers. *Biochim. Et Biophys. Acta Biomembr.* **2018**, *1860*, 319–328. https://doi.org/10.1016/j.bbamem.2017.10.024.
13. Ouyang, H.; Moore, D.J.; Sills, R.H.; Mendelsohn, R. FT-IR studies of sickle hemoglobin interaction with phosphatidylserine. *Spectrosc. Int. J.* **2004**, *18*, 407–413. https://doi.org/10.1155/2004/805318.
14. Huster, D. Solid-state NMR spectroscopy to study protein lipid interactions. *Biochim. Et Biophys. Acta-Mol. Cell Biol. Lipids* **2014**, *1841*, 1146–1160. https://doi.org/10.1016/j.bbalip.2013.12.002.
15. Drücker, P.; Gerke, V.; Galla, H.J. Importance of phospholipid bilayer integrity in the analysis of protein-lipid interactions. *Biochem. Biophys. Res. Commun.* **2014**, *453*, 143–147. https://doi.org/10.1016/j.bbrc.2014.09.079.

16. Bhowmik, D.; Mote, K.R.; MacLaughlin, C.M.; Biswas, N.; Chandra, B.; Basu, J.K.; Walker, G.C.; Madhu, P.K.; Maiti, S. Cell-membrane-mimicking lipid-coated nanoparticles confer Raman enhancement to membrane proteins and reveal membrane-attached amyloid-β conformation. *ACS Nano* **2015**, *9*, 9070–9077. https://doi.org/10.1021/acsnano.5b03175.
17. Tu, A.T. Raman Spectroscopy in Biology: Principles and Applications; John Wiley & Sons Hoboken: Hoboken, NJ, USA, 1982.
18. Ma, H.; Li, L.; Bi, X.; Li, P.; Bao, Y.; Wang, X.; Guo, H.; Chen, Z.; Zhang, W.; Wu, Z.; et al. Surfaced-enhanced Raman spectroscopy (SERS) 50 Years: Theories, applications and perspectives. *J. Light Scatt.* **2025**, *37*, 357–514. https://doi.org/10.13883/j.issn1004-5929.202503001. (In Chinese)
19. Zhu, H.; Zhang, J.; Dai, X.; Mesias, V.S.D.; Chi, H.; Wang, C.; Yeung, C.S.; Chen, Q.; Liu, W.; Huang, J. Tunable lipid-coated nanoporous silver sheet for characterization of protein-membrane interactions by surface-enhanced Raman scattering (SERS). *Anal. Bioanal. Chem.* **2023**, *415*, 3243–3253.
20. Xu, G.; Li, W.; Xie, H.; Zhu, J.; Song, L.; Tang, J.; Miao, Y.; Han, X.X. In situ monitoring of membrane protein electron transfer *via* surface-enhanced resonance Raman spectroscopy. *Anal. Chem.* **2024**, *96*, 6–11. https://doi.org/10.1021/acs.analchem.3c04700.
21. Yin, H.Y.; Vergeade, A.; Shi, Q.; Zackert, W.E.; Gruenberg, K.C.; Bokiej, M.; Amin, T.; Ying, W.Z.; Masterson, T.S.; Zinkel, S.S.; et al. Acetaminophen inhibits cytochrome c redox cycling induced lipid peroxidation. *Biochem. Biophys. Res. Commun.* **2012**, *423*, 224–228. https://doi.org/10.1016/j.bbrc.2012.05.058.
22. Vladimirov, G.K.; Nesterova, A.M.; Levkina, A.A.; Osipov, A.N.; Teselkin, Y.O.; Kovalchuk, M.V.; Vladimirov, Y.A. The dynamics of the formation of cytochrome c complexes with anionic lipids and the mechanism of the production of lipid radicals catalyzed by these complexes. *Biol. Membr.* **2020**, *37*, 287–298. https://doi.org/10.31857/S0233475520040088.
23. Gorbenko, G.P.; Trusova, V.M.; Molotkovsky, J.G.; Kinnunen, P.K.J. Cytochrome c induces lipid demixing in weakly charged phosphatidylcholine/phosphatidylglycerol model membranes as evidenced by resonance energy transfer. *Biochim. Et Biophys. Acta-Biomembr.* **2009**, *1788*, 1358–1365. https://doi.org/10.1016/j.bbamem.2009.03.007.
24. Zhao, J.; Zhao, L.; Xu, W.; Lu, Z.; Xu, S. Fabrication of high-negatively charged bicelle-mediated supported lipid bilayer. *Langmuir* **2024**, *40*, 8083–8093.
25. An, H.H.; Han, W.B.; Kim, Y.; Kim, H.S.; Oh, Y.; Yoon, C.S. Preparation of SERS active Ag nanoparticles encapsulated by phospholipids. *J. Raman Spectrosc.* **2014**, *45*, 292–298. https://doi.org/10.1002/jrs.4461.
26. Giancaspro, J.; Scollan, P.; Rosario, J.; Miller, E.; Braziel, S.; Lee, S. Structural determination of model phospholipid membranes by Raman spectroscopy: Laboratory experiment. *Biochem. Mol. Biol. Educ.* **2022**, *50*, 181–192.
27. Bangham, A.D. Diffusion of univalent ions across the lamellae of swollen phospholipids. Journal of Molecular Biology **1965**, *13*, 238–252.
28. Gaber, B.P.; Peticolas, W.L. Quantitative interpretation of biomembrane structure by Raman-spectroscopy. *Biochim. Et Biophys. Acta-Biomembr.* **1977**, *465*, 260–274. https://doi.org/10.1016/0005-2736(77)90078-5.
29. Chen, X.; Al-Mualem, Z.A.; Baiz, C.R. Lipid Landscapes: Vibrational spectroscopy for decoding membrane complexity. *Annu. Rev. Phys. Chem.* **2024**, *75*, 283–305.
30. Jin, S.; Lednev, I.K.; Jung, Y.M. Recent trends in surface-enhanced Raman spectroscopy-based biosensors: Label-free early disease diagnosis. *J. Phys. Chem. C* **2024**, *128*, 8861–8873. https://doi.org/10.1021/acs.jpcc.4c0201
31. Greig, J.C.; Tipping, W.J.; Graham, D.; Faulds, K.; Gould, G.W. New insights into lipid and fatty acid metabolism from Raman spectroscopy. *Analyst* **2024**, *149*, 4789–4810. https://doi.org/10.1039/D4AN00846D.
32. Li, J.B.; Cheng, W.N.; Wang, X.L.; Zhang, H.J.; Jin, J.; Ji, W.; Han, X.X.; Zhao, B. Electron transfer of Cytochrome c on surface-enhanced Raman scattering-active substrates: material dependence and biocompatibility. *Chem. A Eur. J.* **2017**, *23*, 9034–9038. https://doi.org/10.1002/chem.201702307.
33. Zhu, J.Y.; Jiang, M.W.; Ma, H.; Zhang, H.J.; Cheng, W.N.; Li, J.B.; Cai, L.J.; Han, X.X.; Zhao, B. Redox-State-Mediated Regulation of Cytochrome c Release in Apoptosis revealed by surface-enhanced Raman scattering on Nickel substrates. *Angew. Chem. Int. Ed.* **2019**, *58*, 16499–16503. https://doi.org/10.1002/anie.201909638.
34. Zivanovic, V.; Kochovski, Z.; Arenz, C.; Lu, Y.; Kneipp, J. SERS and cryo-EM directly reveal different liposome structures during interaction with gold nanoparticles. *J. Phys. Chem. Lett.* **2018**, *9*, 6767–6772. https://doi.org/10.1021/acs.jpclett.8b03191.
35. Zivanovic, V.; Seifert, S.; Drescher, D.; Schrade, P.; Werner, S.; Guttmann, P.; Szekeres, G.P.; Bachmann, S.; Schneider, G.; Arenz, C.; et al. Optical nanosensing of lipid accumulation due to enzyme inhibition in live cells. *ACS Nano* **2019**, *13*, 9363–9375. https://doi.org/10.1021/acsnano.9b04001.
36. Zivanovic, V.; Milewska, A.; Leosson, K.; Kneipp, J. Molecular structure and interactions of lipids in the outer membrane of living cells based on surface-enhanced Raman scattering and liposome models. *Anal. Chem.* **2021**, *93*, 10106–10113. https://doi.org/10.1021/acs.analchem.1c00964.
37. Lee, P.C.; Meisel, D. Adsorption and surface-enhanced Raman of dyes on silver and gold sols. *J. Phys. Chem.* **1982**, *86*, 3391–3395.